Geophysical Journal International

Geophys. J. Int. (2020) **223,** 765–776
Advance Access publication 2020 August 19
GJI General Geophysical Methods

doi: 10.1093/gji/ggaa312

Frequency-dependent spherical-wave nonlinear AVO inversion in elastic media

Guangsen Cheng, Xingyao Yin and Zhaoyun Zong

School of Geosciences, China University of Petroleum (East China), Qingdao 266580, Shandong, China. E-mail: xyyin@upc.edu.cn

Accepted 2020 June 22. Received 2020 June 19; in original form 2019 October 30

SUMMARY

The plane-wave reflection coefficient (PRC) plays a remarkable role in conventional amplitude variation with offset (AVO) analysis and inversion. Compared with the widely exploited PRC that breaks down at the near- and supercritical incidence angles, the spherical-wave reflection coefficient (SRC) can overcome the influence of wide-angle reflection and give an accurate description of the actual seismic wave reflection phenomenon based on spherical-wave fronts. However, SRC is not widely used in AVO inversion due to its nonlinearity and computational complexity. In our study, the characteristics of frequency–depth-dependent monochromatic SRC are discussed and a novel three-parameter SRC is derived. Compared with the conventional six-parameter SRC, the novel three-parameter SRC improves the stability of spherical-wave AVO inversion. In addition, the concept of SRC within the Fresnel zone is proposed, and the accuracy of SRC within the Fresnel zone in the deep subsurface is tested. Finally, a nonlinear spherical-wave AVO inversion method for elastic media is proposed, which can make full use of all frequency components of wavelet. The robustness of the proposed method is verified by the application on synthetic seismogram with white Gaussian noise. The feasibility and practicability of this method are verified by comparing the spherical-wave AVO inversion results with the filtered well logs at the known well location.

Key words: Fourier analysis; Wave propagation; Inverse theory; Numerical modelling; Numerical solutions.

1 INTRODUCTION

Plane-wave theory is widely exploited in pre-stack AVO analysis (Ostrander 1984; Rutherford & Williams 1989; Castagna & Swan 1997; Kumar *et al.* 2019) and inversion (Smith & Gidlow 1987; Buland & Omre 2003; Yin & Zhang 2014; Zong *et al.* 2015, 2017; Li *et al.* 2020). Frequency-independent plane-wave reflection coefficients are the essential tools in the estimation of elastic parameters. However, the present widely used linear (Bortfeld 1961; Goodway *et al.* 1997; Aki & Richards 2002; Russell *et al.* 2011) and nonlinear (Wang 1999; Stovas & Ursin 2003; Cheng *et al.* 2017, 2018) plane-wave approximate reflection coefficients are limited by the weak-contrast assumption of interfaces. Even the exact Zoeppritz plane-wave reflection coefficients (Zoeppritz 1919) are derived based on the assumption of plane-wave fronts. In contrast to plane-wave theory, spherical-wave theory can describe the real seismic wave field excited by point source.

To simplify the spherical-wave equations, Sommerfeld (1909) and Weyl (1919) proposed the Sommerfeld integral and Weyl integral, respectively. Later, the simpler formulae of reflected spherical waves for harmonic source and acoustic media were proposed (Červený 1959; Červený & Hron 1961). The first-order and high-order spherical-wave asymptotic equations were given by Brekhovskikh (1980) and Aki & Richards (2002), respectively. It must be noted that the high-order asymptotic equations are not always more accurate than the zeroth- or first-order asymptotic equations. One conventional approach to obtain the exact SRC is full-wave numerical simulation (Alhussain *et al.* 2008; Zhu & McMechan 2012), for instance, the finite difference method. Another widely exploited approach to obtain the exact SRC is the weighted integral of the PRC (Ursenbach *et al.* 2007; Ayzenberg *et al.* 2009). The weighted integral method is under the assumption of the particle motions of compressional wave and shear wave are in the same and perpendicular directions to the wave propagation, respectively. Haase & Ursenbach (2006) verified the error caused by the assumption is small and negligible.

The SRC is dependent on not only the incidence angles and elastic parameters between layers but also the frequency and the distances between source, receiver and reflection point (Li *et al.* 2017a). Seismic reflection information can improve the accuracy of density inversion at near-critical incident angle and supercritical incident angle. The SRC overcomes the error caused by the PRC at large incidence angles. In addition, the SRC can make full use of the amplitude, frequency, and propagation distance to estimate the elastic parameters. However, its nonlinearity and computational complexity limit its practical application. The frequency components of seismic data have been used in the

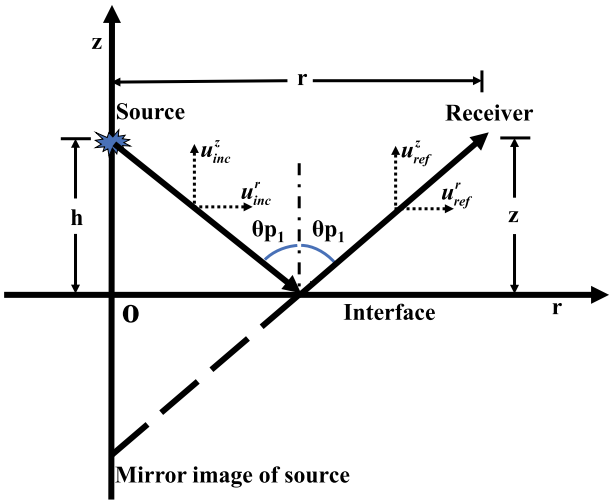

Figure 1. A single plane interface between two half-spaces in elastic media.

conventional plane-wave AVO inversion (Kroode *et al.* 2013; Zong *et al.* 2018; Cheng *et al.* 2019). In recent years, the frequency-dependent SRC has attracted more and more attention. The single-frequency spherical-wave AVO inversion of elastic media (Krail & Brysk 1983; Skopintseva *et al.* 2011) and the multi-frequency spherical-wave AVO inversion of acoustic media (Li *et al.* 2017b) have been studied intensively.

Previous researches on spherical-wave AVO inversion mainly utilized SRC with one or several frequency components, which could not make full use of all frequency information of actual seismic wavelet. A single plane interface between two half-spaces rather than multilayer interface usually was designed for spherical-wave AVO inversion. In addition, conventional SRC needs to estimate six parameters (compressional wave velocity, shear wave velocity, and density in the upper and lower media) simultaneously. Too many unknown parameters bring great challenges to the stability of spherical-wave AVO inversion. In view of these problems, we propose a frequency-dependent spherical-wave nonlinear AVO inversion method to fully utilize the frequency components within the bandwidth of actual band-limited wavelet. Moreover, the method can also achieve the estimation of elastic parameters in multilayer media, which promotes the practical application of spherical-wave AVO inversion. To improve the stability of spherical-wave AVO inversion, an exact plane-wave reflection coefficient equation with three parameters (*P*-wave velocity reflectivity, *S*-wave velocity reflectivity, and density reflectivity) are substituted into the conventional SRC, and a novel three-parameter SRC is obtained. In consideration of the complexity and non-analyticity of the SRC, the nonlinear inversion algorithm proposed by Růžek *et al.* (2009) is utilized in this paper. We also derive the SRC within the Fresnel zone that plays an essential role in seismic exploration, especially in the spatial lateral resolving power and the description of reflected and transmitted wave fields (Ursin *et al.* 2014).

2 THE COMPUTATION AND ANALYSIS OF MONOCHROMATIC SRC

A single plane interface between two half-spaces in Fig. 1 describes the incident and reflected elastic spherical compressional wave (*P*-wave). We assume that the displacement of the spherical *P*-wave particle motion has the same direction as the wave propagation and other displacement components are negligible (Haase & Ursenbach 2006). The receiver and the source are at the same depth.

In Fig. 1, the mirror image of the *P*-wave source excites the monochromatic spherical wave. The displacement potential of the incident spherical wave at the receiver point can be expressed as (Aki & Richards 2002)

$$\phi_{\text{inc}} = A\text{i}\omega \exp(-\text{i}\omega t) \int_0^\infty \frac{p}{\xi} J_0(\omega p r) \exp[\text{i}\omega\xi(z+h)]\,\text{d}p, \tag{1}$$

and the displacement potential of the reflected spherical wave at the receiver point is

$$\phi_{\text{ref}} = A\text{i}\omega \exp(-\text{i}\omega t) \int_0^\infty R_{\text{pp}} \frac{p}{\xi} J_0(\omega p r) \exp[\text{i}\omega\xi(z+h)]\,\text{d}p, \tag{2}$$

where i, t ω are the imaginary unit, time and angular frequency, respectively. The constant A is decided by the source strength. J_0 is the zero-order Bessel function. r is the horizontal distance between the source and the receiver. z and h are the vertical distances between the receiver, the source and the interface, respectively. The product of A, i, ω and the integral of p is the amplitude (strength) of the spherical-wave displacement potential. The incident spherical-wave displacement can be expressed as

$$\boldsymbol{u}_{\text{inc}}\left(u^r_{\text{inc}}, u^z_{\text{inc}}\right) = \nabla\phi_{\text{inc}} = \left(\frac{\partial\phi_{\text{inc}}}{\partial r}, \frac{\partial\phi_{\text{inc}}}{\partial z}\right), \tag{3}$$

Table 1. Model 1.

Stratum	V_p (m s^{-1})	V_s (m s^{-1})	ρ (g cm^{-3})
Shale	2000	880	2.400
Sand	2933	1882	2.000

Table 2. Model 2.

Stratum	V_p (m s^{-1})	V_s (m s^{-1})	ρ (g cm^{-3})
Shale	2898	1290	2.425
Gas bearing sandstone	2857	1666	2.275

$u^r_{\rm inc}$ and u^z_{inc} are the displacement components of the incident wave in the radial direction and vertical direction, respectively. The reflected spherical-wave displacement is

$$\boldsymbol{u}_{\rm ref}\left(u^r_{\rm ref}, u^z_{\rm ref}\right) = \nabla\phi_{\rm ref} = \left(\frac{\partial\phi_{\rm ref}}{\partial r}, \frac{\partial\phi_{\rm ref}}{\partial z}\right), \tag{4}$$

$u^r_{\rm ref}$ and $u^z_{\rm ref}$ are the displacement components of the reflected wave in the radial direction and vertical direction, respectively. The incident spherical-wave displacement in the ray direction can be expressed as

$$u_{\rm inc} = u^r_{\rm inc}\sin\theta_{p1} + u^z_{\rm inc}\cos\theta_{p1} = \frac{\partial\phi_{\rm inc}}{\partial r}\sin\theta_{p1} + \frac{\partial\phi_{\rm inc}}{\partial z}\cos\theta_{p1} = A_{\rm inc}\exp(-{\rm i}\omega t), \tag{5}$$

where $A_{\rm inc} = A{\rm i}\omega^2\int_0^{+\infty}\frac{p}{\xi}[-pJ_1(\omega pr)\sin\theta + {\rm i}\xi J_0(\omega pr)cos\theta]exp(i\omega\xi(z+h)){\rm d}p$, J_1 is the first-order Bessel function. The reflected spherical-wave displacement can be expressed as

$$u_{\rm ref} = u^r_{\rm ref}\sin\theta_{p1} + u^z_{\rm ref}\cos\theta_{p1} = \frac{\partial\phi_{\rm ref}}{\partial r}\sin\theta_{p1} + \frac{\partial\phi_{\rm ref}}{\partial z}\cos\theta_{p1} = A_{\rm ref}\exp(-{\rm i}\omega t), \tag{6}$$

where

$$A_{\rm ref} = A{\rm i}\omega^2\int_0^{+\infty} R_{\rm pp}\frac{p}{\xi}\left[-pJ_1(\omega pr)sin\theta + {\rm i}\xi J_0(\omega pr)\cos\theta\right]\exp({\rm i}\omega\xi(z+h))\,{\rm d}p.$$

$A_{\rm inc}$ and $A_{\rm ref}$ are the incident and reflected spherical-wave amplitudes, respectively. Spherical diffusion makes A_{inc} and A_{ref} decrease with the increase of propagation distance, and its influence can be eliminated by the ratio of A_{ref} to A_{inc}. The monochromatic compressional SRC can be written as

$$R^{\rm sph}_{\rm pp} = \frac{A_{\rm inc}}{A_{\rm ref}} = \frac{\int_0^{+\infty} R_{\rm pp}\frac{p}{\xi}\left[-pJ_1(\omega pr)\sin\theta + {\rm i}\xi J_0(\omega pr)\cos\theta\right]\exp({\rm i}\omega\xi(z+h))\,{\rm d}p}{\int_0^{+\infty}\frac{p}{\xi}\left[-pJ_1(\omega pr)\sin\theta + {\rm i}\xi J_0(\omega pr)\cos\theta\right]\exp(i\omega\xi(z+h))\,{\rm d}p}. \tag{7}$$

The singular point ($p = \frac{1}{v_{p1}}$) in the integral path brings difficulties to calculate eq. (7). We refer to the research of Ursenbach *et al.* (2007). Substituting $\xi = \frac{\cos\theta_{p1}}{v_{p1}}$, $\frac{p}{\xi}dp = -\frac{d\cos\theta_{p1}}{v_{p1}}$, and $x = \cos\theta_{p1}$ into eq. (7), the equation can be further written as

$$R^{\rm sph}_{\rm pp} = \frac{\left[\int_1^0 R_{\rm pp}(x)J_a\exp\left({\rm i}\omega\frac{x}{vp_1}(z+h)\right){\rm d}x + {\rm i}\int_0^{+\infty} R_{\rm pp}({\rm i}x)J_b\exp\left(-\omega\frac{x}{vp_1}(z+h)\right){\rm d}x\right]}{\left[\int_1^0 J_a\exp\left(i\omega\frac{x}{vp_1}(z+h)\right){\rm d}x + {\rm i}\int_0^{+\infty} J_b\exp\left(-\omega\frac{x}{vp_1}(z+h)\right){\rm d}x\right]}, \tag{8}$$

with $J_a = -\frac{\sqrt{1-x^2}}{vp_1}J_1(\omega\frac{\sqrt{1-x^2}}{vp_1}r)\sin\theta_{p1} + {\rm i}\frac{x}{vp_1}J_0(\omega\frac{\sqrt{1-x^2}}{vp_1}r)\cos\theta_{p1}$ and $J_b = -\frac{\sqrt{1+x^2}}{vp_1}J_1(\omega\frac{\sqrt{1+x^2}}{vp_1}r)\sin\theta_{p1} - \frac{x}{vp_1}J_0(\omega\frac{\sqrt{1+x^2}}{vp_1}r)\cos\theta_{p1}$.

The Gauss–Kronrod algorithm (Shampine 2008) and two models are utilized to calculate the SRC. Tables 1 and 2 display the elastic parameters of model 1 (Haase 2004) and model 2 (Goodway *et al.* 1997), respectively. Models 1 and model 2 are two kinds of typical models that can reflect the characteristics of spherical wave reflection coefficients. Velocities increase across the reflected interface in model 1 that constitutes a Class I AVO. The critical angle (43°) only exists in model 1 and head waves can be generated from reflected waves. The elastic parameters in model 2 are from an actual gas well and there are no critical angles and head waves.

Figs 2 and 3 display the (a) amplitude and (b) phase of the SRC and PRC variation with incidence angles calculated by model 1. Compared to Figs 2 and 3, model 2 is utilized in Figs 4 and 5. Figs 2 and 4 display the monochromatic SRC with different frequencies when z (the vertical distances between the receiver and the interface) is set to 500 m. The curves in cyan, green, and blue represent the monochromatic SRC of 5 Hz, 30 Hz, and 90 Hz, respectively. Figs 3 and 5 display the 30 Hz monochromatic SRC when z equals to 200 m (cyan curves), 1000 m (green curves), and 4000 m (blue curves), respectively. The red curves represent the PRC. It can be seen from Figs. 2 to Fig. 5 that the SRC is frequency–depth dependent, but the PRC is not. For model 1 (Figs 2 and 3), the biggest difference between the SRC and the PRC nears the critical incident angle. The amplitude oscillations of SRC caused by head waves (Červený & Hron 1961) occur after the critical angle. For model 2 (Figs 4 and 5), there are no critical angle and head waves. The difference between SRC and PRC is very small. We can conclude that the PRC is closer to the SRC with the increase of propagating distance and frequency.

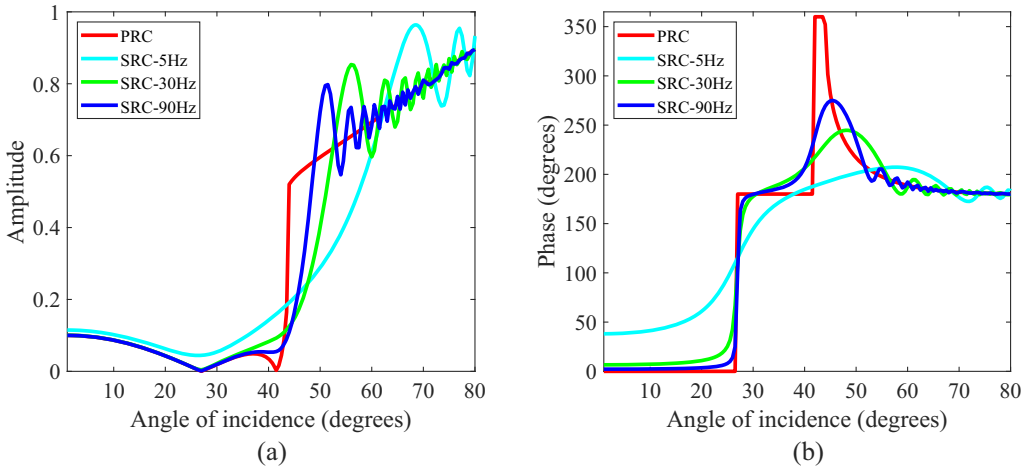

Figure 2. The (a) amplitude and (b) phase of the monochromatic SRC variation with incidence angles at different frequencies calculated by model 1.

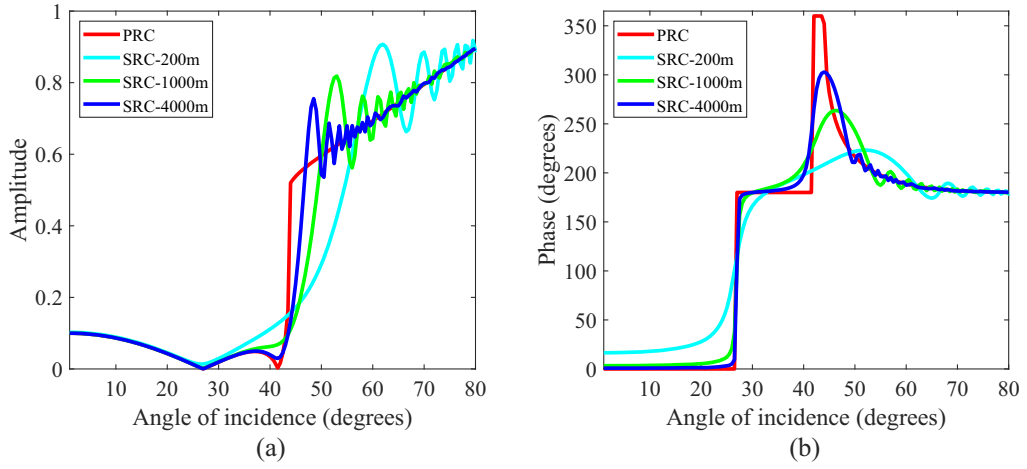

Figure 3. The (a) amplitude and (b) phase of the monochromatic SRC variation with incidence angles at different propagation distances calculated by model 1.

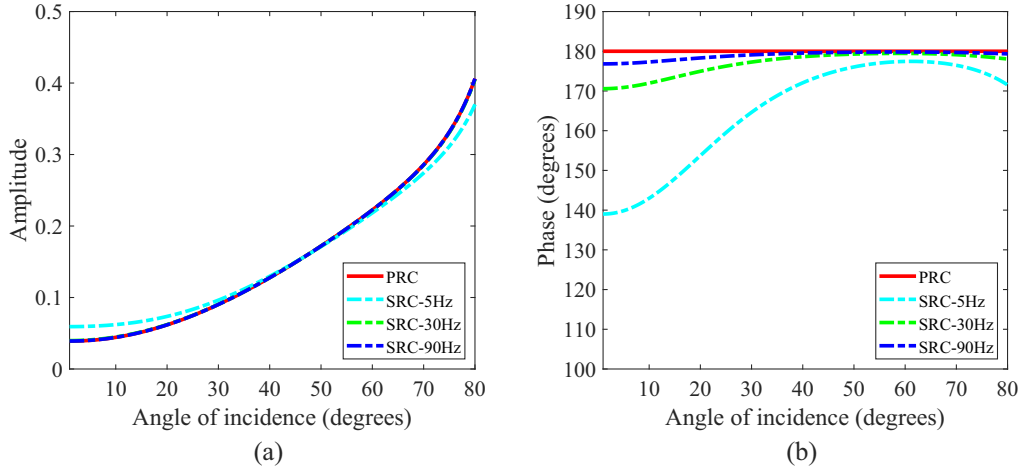

Figure 4. The (a) amplitude and (b) phase of the monochromatic SRC variation with incidence angles at different frequencies calculated by model 2.

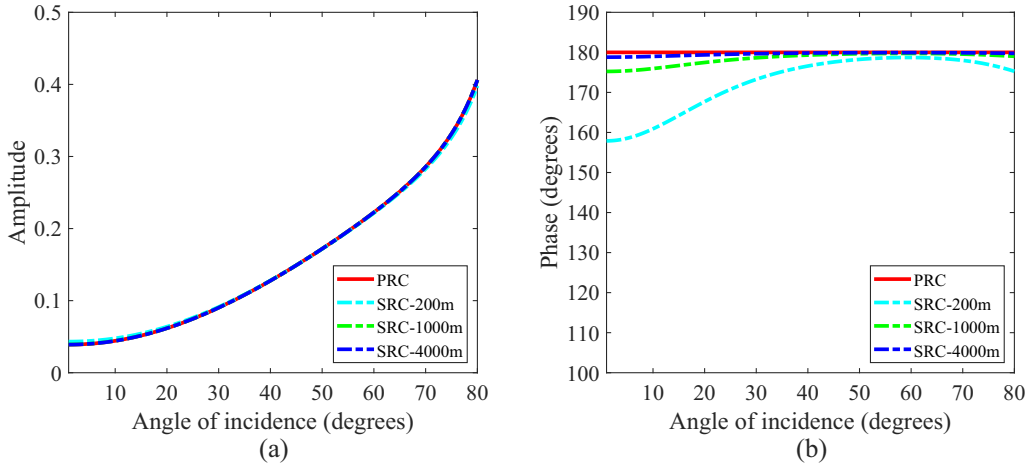

Figure 5. The (a) amplitude and (b) phase of the monochromatic SRC variation with incidence angles at different propagation distances calculated by model 2.

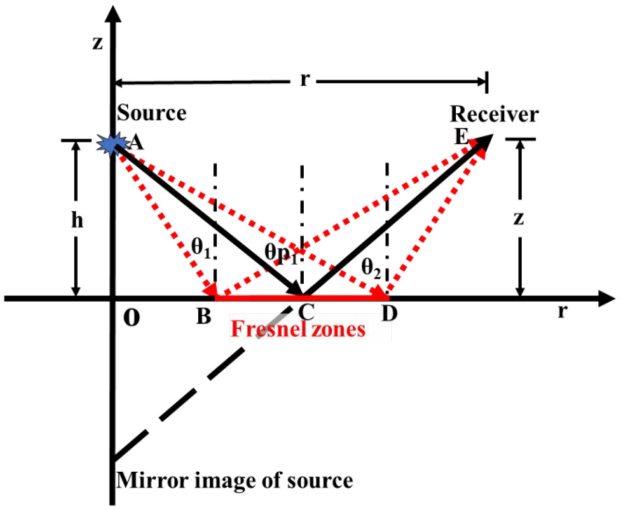

Figure 6. The first-order Fresnel zone at the non-zero incidence angles.

3 MONOCHROMATIC SPHERICAL-WAVE AVO WITHIN THE FRESNEL ZONE

The Fresnel zone contributes to the spatial lateral resolving power (Sheriff 1980; Yilmaz 2001), the construction of observation system (Goertz *et al.* 2005), the identification of geological abnormity body, and the amplitudes of reflected wavefields (Spetzler & Snieder 2004; Favretto-Cristini *et al.* 2007). We derive a monochromatic SRC within the Fresnel zone and aim to emphasize its contributions to the reflected spherical wavefield in the deep subsurface of the Earth.

In Fig. 6, the incidence angle is θ_{p1} and the reflection point is C. The BD in red represents the reflector within the first-order Fresnel zone. The ABE and ADE (red dotted lines) are the boundaries of the propagation path of the reflected wave within the first-order Fresnel zone. According to the relation between wavelength (λ) and propagation distanceACE($2l$), we can derive the formulae of $\mathrm{ABE}-\mathrm{ACE}=\frac{\lambda}{2}$ and $\mathrm{ADE}-\mathrm{ACE}=\frac{\lambda}{2}$. The length of BC and CD can be derived and expressed as

$$\mathrm{BC}=\mathbf{CD}=\sqrt{\frac{\left(\frac{\lambda l}{2}+\frac{\lambda^2}{16}\right)\left(l+\frac{\lambda}{4}\right)^2}{\sin^2\theta_{p1}\left(\frac{\lambda l}{2}+\frac{\lambda^2}{16}\right)+\cos^2\theta_{p1}\left(l+\frac{\lambda}{4}\right)^2}}. \tag{9}$$

The $\cos\theta_1$ and $\cos\theta_2$ can be further obtained and written as

$$\cos\theta_1=\frac{h}{\mathrm{AB}}=\frac{h}{\sqrt{h^2+(\mathrm{OC}-\mathrm{BC})^2}}=\frac{h}{\sqrt{h^2+\left(h\tan\theta_{p1}-\mathrm{BC}\right)^2}}, \tag{10}$$

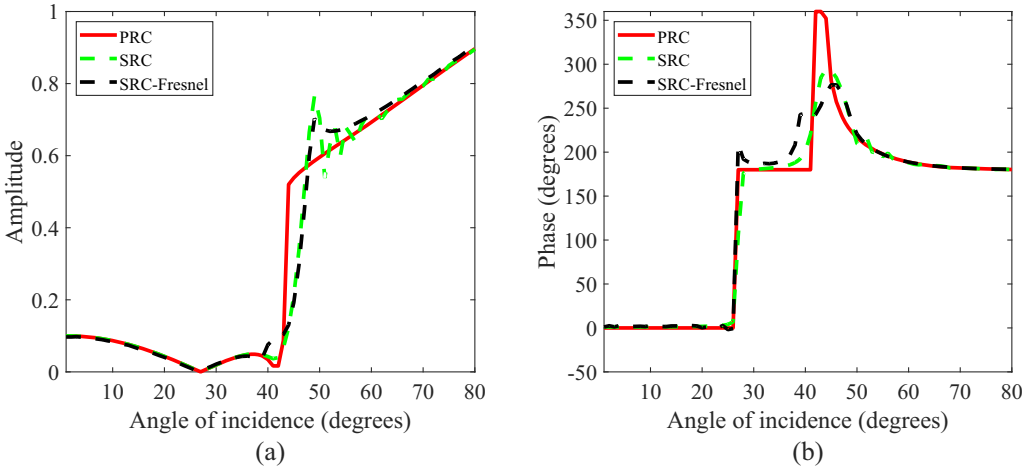

Figure 7. The (a) amplitude and (b) phase of the monochromatic SRC variation with the incident angles within the Fresnel zone calculated by model 1.

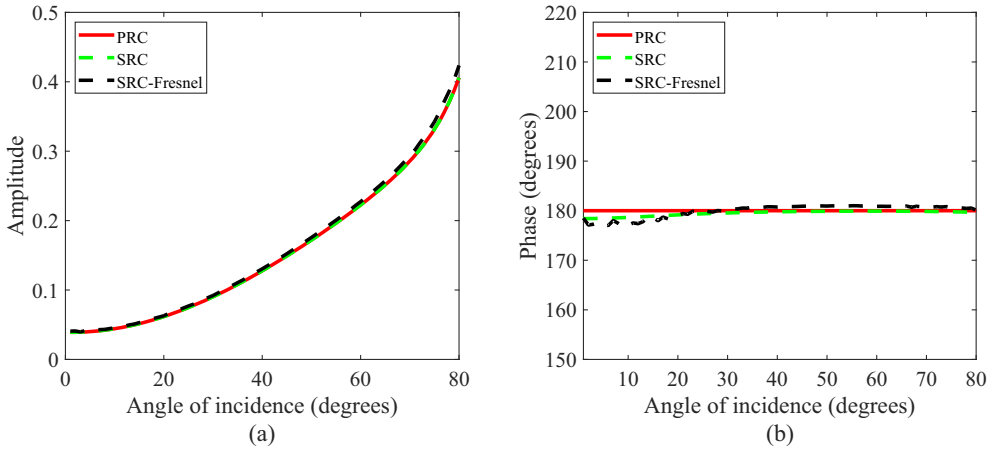

Figure 8. The (a) amplitude and (b) phase of the monochromatic SRC variation with the incident angles within the Fresnel zone calculated by model 2.

and

$$\cos\theta_2 = \frac{h}{\mathrm{AD}} = \frac{h}{\sqrt{h^2 + (\mathrm{OC} + \mathrm{CD})^2}} = \frac{h}{\sqrt{h^2 + \left(h\tan\theta_{p1} + \mathrm{CD}\right)^2}}. \tag{11}$$

Changing the integral range by substituting eq. (10) and eq. (11) into the integral domain of eq. (8), the SRC within the Fresnel zone can be obtained. Models 1 and model 2 are used. Thezand frequency are set to 3000 m and 30 Hz, respectively.

Figs 7 and 8 display the (a) amplitude and (b) phase of monochromatic SRC within the Fresnel zone calculated by model 1 and model 2, respectively. The curves in red, green, and black represent the PRC, SRC, and SRC within the Fresnel zone respectively. From Fig. 7 we can see that the monochromatic SRC within the Fresnel zone has higher accuracy in contrast to the PRC. The differences between the SRC within the Fresnel zone and the SRC are mainly concentrated at the near-critical incidence angles. Fig. 8 shows that the amplitude and phase of SRC within the Fresnel zone basically coincide with the SRC. The SRC within the first-order Fresnel zone has high accuracy, which is helpful to study the reflected spherical wavefield in the deep subsurface of the Earth.

4 THE FORWARD MODELLING OF SPHERICAL WAVE

The amplitude and phase of SRC will be influenced by the monochromatic spherical waves of different frequencies during the seismic wave propagation. With the same incidence angle, propagation distance, and elastic parameters between layers, the SRC is only dependent on the frequency. To make full use of the frequency components of seismic wavelet, the band-limited wavelet can be decomposed into the monochromatic spherical waves with different frequencies. As shown in Figs 2–5, the monochromatic spherical waves with different frequencies have different reflection coefficient curves. That is to say, there is a one-to-one mapping between SRC and frequency components. The high-frequency components make spherical wave closer to the plane wave, and the influence of low-frequency components on AVO cannot also be ignored. The SRC is regarded as the filter or weighting factor of the band-limited spherical waves in the frequency domain. The spherical reflection waveform can be obtained by the inverse Fourier transform to the calculations for all frequency points (Haase 2004).

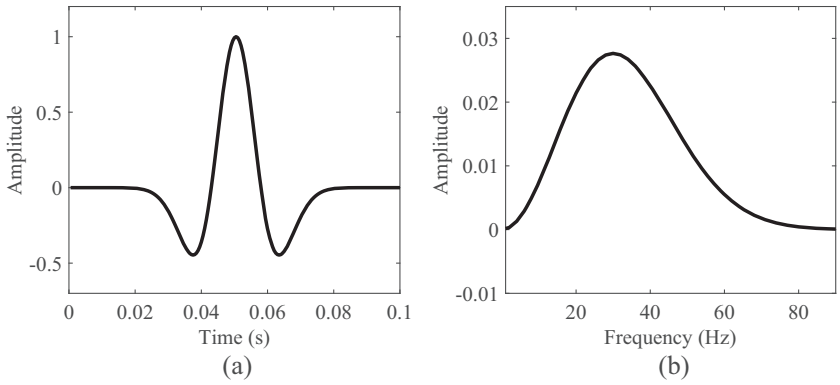

Figure 9. The band-limited Ricker wavelet in the time domain and frequency domain.

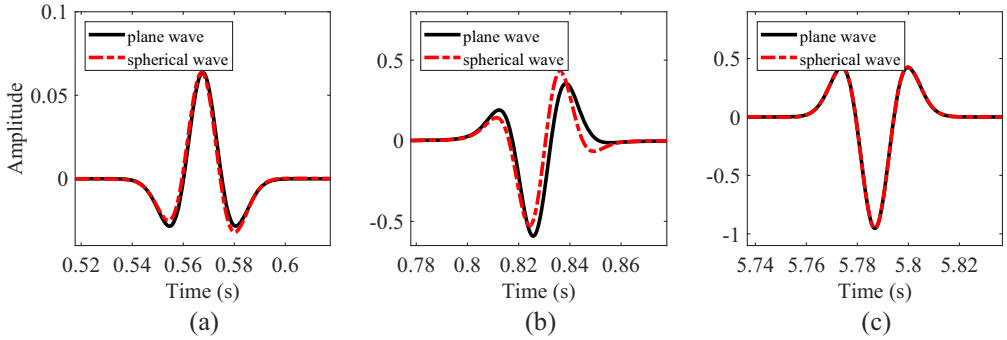

Figure 10. The spherical-wave reflection waveform (black solid) and the plane-wave reflection waveform (dashed red) calculated by model 1 at the (a) pre-critical incident angle (15°), (b) near-critical incident angle (50°) and (c) post-critical incident angle (80°).

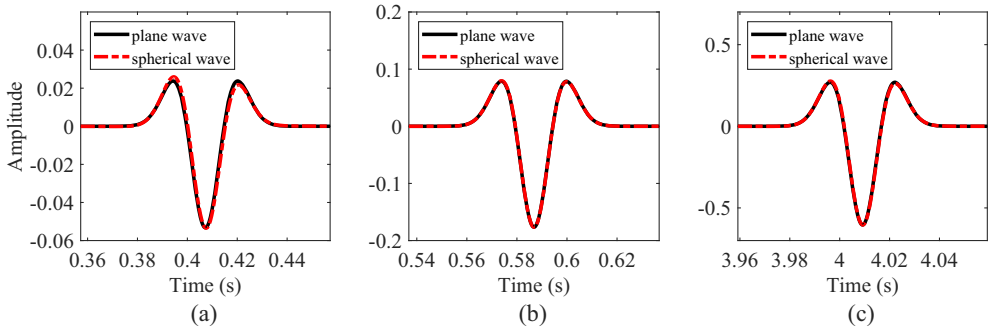

Figure 11. The spherical-wave reflection waveform (black solid) and the plane-wave reflection waveform (red dashed) calculated by model 2 at the incident angles of (a) 15°, (b) 50°, and (c) 85°. (There is no critical incident angle.)

In this paper, a band-limited Ricker wavelet (the dominant frequency is 30 Hz) and model 1 (Table 1) are employed in the calculation of spherical reflection waveform and finite difference modelling.

Figs 9(a) and (b) display the band-limited Ricker wavelet in the time domain and frequency domain, respectively. The critical angle is 43° and $z$is 500 m. The plane-wave reflection waveform is also derived via the inverse Fourier transform. Figs 10(a)–(c) display the differences between the spherical-wave reflection waveform (black solid) and the plane-wave reflection waveform (red dashed) at the pre-critical incidence angle of 15°, near-critical incidence angle of 50°, and post-critical incidence angle of 85°, respectively. Compared with the PRC, the SRC is frequency-dependent, and there are slight differences between the spherical-wave reflection waveform and the plane-wave reflection waveform at the pre-critical incidence angles. There are significant differences caused by head waves at the near-critical incident angles. At the post-critical incident angles, the spherical-wave reflection waveform and the plane-wave reflection waveform are almost same. Figs 11(a)–(c) display the spherical-wave reflection waveform (black solid) and the plane-wave reflection waveform (red dashed) calculated by model 2 at the incident angles of 15°, 50°, and 85°, respectively. There are subtle, or even no differences between the spherical-wave reflection waveform and the plane-wave reflection waveform.

For demonstrating the accuracy and credibility of the band-limited spherical-wave reflection waveform, the elastic wave finite difference (FD) modelling is implemented to calculate the reflection waveform at the pre-critical incidence angle of 15°. Once again, the single plane interface between two half-spaces in Fig. 1 is utilized. During the forward modelling of spherical waves, we don't consider the free surface

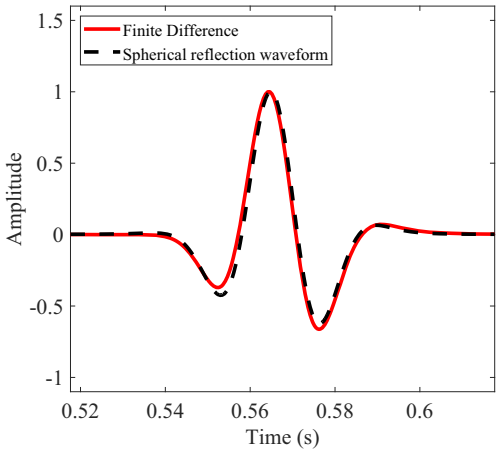

Figure 12. The normalized reflection waveforms calculated by the band-limited spherical wave (black dotted curve) and the elastic wave finite difference modelling (red solid curve).

effects. In addition, the *P*-wave point source in elastic media and the planar reflection interface are assumed (as shown in Fig. 1). The simple one reflection interface in elastic media is sufficient to verify the feasibility of our method to obtain band-limited spherical waves. Haase & Ursenbach (2007) and Ayzenberg *et al.* (2009) further studied on the spherical wave reflection coefficient for anelastic media and curved interfaces, respectively. The frequencies of incident waves should be within the seismic-frequency range. The depth of reflection interface needs to be set first because of the spherical wave AVO is depth-dependent. The Perfect Matched Layer (PML) absorbing boundary condition (Berenger 1994) is used to eliminate the boundary reflections.

In Fig. 12, the curves in black and red represent the reflection waveforms (after normalization) obtained from the band-limited spherical wave and the finite difference modelling, respectively. It can be seen that the spherical-wave reflection waveform is agreement well with the simulation results of FD.

5 BAND-LIMITED SPHERICAL-WAVE AVO INVERSION

Six unknown elastic parameters in Zoeppritz *P*-wave reflection coefficient increase the uncertainty and difficulty of spherical-wave AVO inversion. A novel exact PRC with three elastic parameters was proposed (Yin *et al.* 2018) and can be expressed as

$$R_{\mathrm{pp}}^{\mathrm{novel}} = \frac{e_1 f_1 - g_1 h_1}{e_2 f_2 + g_2 h_2}, \tag{12}$$

where

$$e_1 = \frac{2+\frac{\Delta v_p}{v_p}}{2-\frac{\Delta v_p}{v_p}}\cos\theta_{p1}\left[\frac{2+\frac{\Delta\rho}{\rho}}{2-\frac{\Delta\rho}{\rho}}\left(1-2\sin^2\theta_{s2}\right)+2\sin^2\theta_{s1}\right]-\cos\theta_{p2}\left[\left(1-2\sin^2\theta_{s1}\right)+2\frac{2+\frac{\Delta\rho}{\rho}}{2-\frac{\Delta\rho}{\rho}}\sin^2\theta_{s2}\right],$$

$$e_2 = \frac{2+\frac{\Delta v_p}{v_p}}{2-\frac{\Delta v_p}{v_p}}\cos\theta_{p1}\left[\frac{2+\frac{\Delta\rho}{\rho}}{2-\frac{\Delta\rho}{\rho}}\left(1-2\sin^2\theta_{s2}\right)+2\sin^2\theta_{s1}\right]+\cos\theta_{p2}\left[\left(1-2\sin^2\theta_{s1}\right)+2\frac{2+\frac{\Delta\rho}{\rho}}{2-\frac{\Delta\rho}{\rho}}\sin^2\theta_{s2}\right],$$

$$f_1 = f_2 = \left(\frac{2+\frac{\Delta v_p}{v_p}}{2-\frac{\Delta v_s}{v_s}}\right)\frac{v_{\mathrm{p}}}{v_s}\cos\theta_{s1}\left[\frac{2+\frac{\Delta\rho}{\rho}}{2-\frac{\Delta\rho}{\rho}}\left(1-2\sin^2\theta_{s2}\right)+2\sin^2\theta_{s1}\right]+\left(\frac{2+\frac{\Delta v_p}{v_p}}{2+\frac{\Delta v_s}{v_s}}\right)\frac{v_{\mathrm{p}}}{v_s}\cos\theta_{s2}\left[\left(1-2\sin^2\theta_{s1}\right)+2\frac{2+\frac{\Delta\rho}{\rho}}{2-\frac{\Delta\rho}{\rho}}\sin^2\theta_{s2}\right],$$

$$g_1 = \sin^2\theta_{p2}\left[\frac{2+\frac{\Delta\rho}{\rho}}{2-\frac{\Delta\rho}{\rho}}\left(1-2\sin^2\theta_{s2}\right)-\left(1-2\sin^2\theta_{s1}\right)+2\cos\theta_{p1}\cos\theta_{s2}\left(\frac{2+\frac{\Delta\rho}{\rho}}{2-\frac{\Delta\rho}{\rho}}\frac{2+\frac{\Delta v_s}{v_s}}{\left(2-\frac{\Delta v_p}{v_p}\right)\frac{v_p}{v_s}}-\frac{\left(2-\frac{\Delta v_s}{v_s}\right)^2}{\left(2-\frac{\Delta v_p}{v_p}\right)\left(2+\frac{\Delta v_s}{v_s}\right)\frac{v_p}{v_s}}\right)\right],$$

$$g_2 = \sin^2\theta_{p2}\left[\frac{2+\frac{\Delta\rho}{\rho}}{2-\frac{\Delta\rho}{\rho}}\left(1-2\sin^2\theta_{s2}\right)-\left(1-2\sin^2\theta_{s1}\right)-2\cos\theta_{p1}\cos\theta_{s2}\left(\frac{2+\frac{\Delta\rho}{\rho}}{2-\frac{\Delta\rho}{\rho}}\frac{2+\frac{\Delta v_s}{v_s}}{\left(2-\frac{\Delta v_p}{v_p}\right)\frac{v_p}{v_s}}-\frac{\left(2-\frac{\Delta v_s}{v_s}\right)^2}{\left(2-\frac{\Delta v_p}{v_p}\right)\left(2+\frac{\Delta v_s}{v_s}\right)\frac{v_p}{v_s}}\right)\right],$$

$$h_1 = h_2 = \frac{2+\frac{\Delta\rho}{\rho}}{2-\frac{\Delta\rho}{\rho}}\left(1-2\sin^2\theta_{s2}\right)-\left(1-2\sin^2\theta_{s1}\right)-2\cos\theta_{p2}\cos\theta_{s1}\left(\frac{2+\frac{\Delta\rho}{\rho}}{2-\frac{\Delta\rho}{\rho}}\frac{\left(2+\frac{\Delta v_s}{v_s}\right)^2}{\left(2+\frac{\Delta v_p}{v_p}\right)\left(2-\frac{\Delta v_s}{v_s}\right)\frac{v_p}{v_s}}-\frac{2-\frac{\Delta v_s}{v_s}}{\left(2+\frac{\Delta v_p}{v_p}\right)\frac{v_p}{v_s}}\right),$$

$\frac{\Delta v_p}{v_p}=\frac{v_{p2}-v_{p1}}{v_{p2}+v_{p1}}$ is the *P*-wave velocity reflectivity, $\frac{\Delta v_s}{v_s}=\frac{v_{s2}-v_{s1}}{v_{s2}+v_{s1}}$ is the *S*-wave velocity reflectivity and $\frac{\Delta\rho}{\rho}=\frac{\rho_2-\rho_1}{\rho_2+\rho_1}$ is the density reflectivity. Substituting eq. (12) into eq. (8), the novel SRC can be expressed as

$$R_{\mathrm{pp}}^{\mathrm{sph}} = \frac{\left[\int_1^0 R_{\mathrm{pp}}^{\mathrm{novel}}(x)J_a exp\left(\mathrm{i}\omega\frac{x}{vp_1}(z+h)\right)\mathrm{d}x+\mathrm{i}\int_0^{+\infty}R_{\mathrm{pp}}^{\mathrm{novel}}(\mathrm{i}x)J_b\exp\left(-\omega\frac{x}{vp_1}(z+h)\right)\mathrm{d}x\right]}{\left[\int_1^0 J_a\exp\left(\mathrm{i}\omega\frac{x}{vp_1}(z+h)\right)\mathrm{d}x+\mathrm{i}\int_0^{+\infty}J_b exp\left(-\omega\frac{x}{vp_1}(z+h)\right)\mathrm{d}x\right]}. \tag{13}$$

The z, h and elastic parameters in layer 1 are assumed to be known. Meanwhile, the novel SRC (Eq. 13) can overcome the influence of impedance contrast, because eq. (12) is not under the assumption of weak-contrast.

Table 3. The elastic parameters of real gas-bearing sandstone.

Stratum	V_m (m s^{-1})	V_s (m s^{-1})	ρ (g cm^{-3})
Shale	4010	2120	2.304
Gas bearing sandstone	5040	2980	2.446

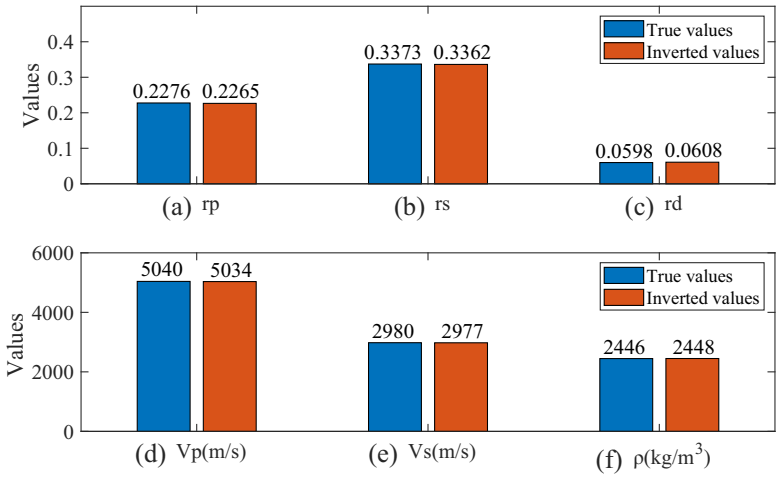

Figure 13. The spherical-wave AVO inversion results without noise.

The objective function of spherical wave AVO inversion can be expressed as

$$F = \left\| \sum_{\omega=\mathrm{LF}}^{\mathrm{HF}} W(\omega) \cdot R_{\mathrm{pp}}^{\mathrm{sph}}(\omega) - d_{\mathrm{obs}} \right\|_2^2 = \mathrm{G}(\mathbf{m}), \tag{14}$$

where $W(\omega)$ is the harmonic wave at the frequency of ω, $\mathbf{m}$=$[rp, rs, rd]$. LF and HF are the lowest and highest frequencies in the frequency band range of wavelet, respectively. Compared with conventional SRC, only rp,rs and rd need to be inverted in Eq. (14), the three-parameter SRC improves the stability of spherical-wave AVO inversion. The band-limited spherical-wave reflection waveform is calculated with the elastic parameters from real gas-bearing sandstone (Table 3) and can be used as the observation data d_{obs} for inversion. To estimate the rp,rs and rd, the spherical-wave AVO inversion method based on the actual band-limited wavelet and frequency-dependent SRC is proposed. The wavelet is decomposed into harmonic waves with different frequencies, and each frequency has a unique weighting factor (SRC). The frequency components within the bandwidth of the band-limited wavelet can be utilized fully.

A powerful nonlinear inversion tool (Růžek *et al.* 2009) is used to solve Eq. (14). The first step is to define the scope of model $\mathbf{m}$ ($\mathbf{m}$=$[rp, rs, rd]$) and select a centre model $\mathbf{m^c}$ randomly. The second step is to obtain the candidate model $\mathbf{m^g}$, $\mathbf{m^g} = \mathbf{m^c} + R\mathbf{Lg}$. The constant R is less than the distance between the centre model and boundary. $\mathbf{g}$is the unit vector. We calculate $\mathbf{L}$ by the Cholesky decomposition of $\mathbf{C^m}$, where $\mathbf{C^m}$= $\mathbf{LL^T} = \begin{bmatrix} \Delta rp^2 & & \\ & \Delta rs^2 & \\ & & \Delta rd^2 \end{bmatrix}$, $\Delta rp = rp^{\max} - rp^{\min}$, $\Delta rs = rs^{\max} - rs^{\min}$, and $\Delta rd = rd^{\max} - rd^{\min}$. The third step is to predict the model $\mathbf{m}_n$=$[rp_{\mathrm{new}}, rs_{\mathrm{new}}, rd_{\mathrm{new}}]$ by kriging, radial basis function network, and linear regression. The last step is to compare $G(\mathbf{m}_n)$ and $G(\mathbf{m}^c)$. If $G(\mathbf{m}_n) \leq G(\mathbf{m}^c)$ and $G(\mathbf{m}_n)$ can meet accuracy requirement, $\mathbf{m}_n$ becomes the centre model. If $G(\mathbf{m}_n) > G(\mathbf{m}^c)$, returning to step 2.

To avoid the influence of the critical angle and head waves, the pre-critical synthetic data is used in the spherical-wave AVO inversion. The synthetic data with white Gaussian noise is further implemented to demonstrate that even under the noise situation, the reasonable inversion results can still be obtained using our method. The plane-wave AVO inversion results based on Zoeppritz equation are given for comparison.

Figs 13 and 14 display the spherical-wave AVO inversion results without and with white Gaussian noise, respectively. The colour bars in blue and red are the true values and inversion results, respectively. (a)–(c) display the *P*-wave velocity reflectivity (rp), *S*-wave velocity reflectivity (rs) and density reflectivity (rd) respectively. (d)–(f) display the *P*-wave velocity (v_p), *S*-wave velocity (v_s) and density (ρ) calculated by the inverted rp, rs and rd. From Figs 13 and 14 we can see that the spherical-wave AVO inversion results without and with white Gaussian noise are highly consistent with the elastic parameters of real gas-bearing sandstone, which verifies the accuracy of our method. In the noise situation, the plane-wave AVO inversion results based on the Zoeppritz equation in Fig. 15 are given for comparison. The colour bars in blue, red, and yellow represent the true values, the spherical-wave inversion results, and the plane-wave inversion results based on the Zoeppritz equation, respectively. From Fig. 15 we can see that the spherical-wave AVO inversion results are better than the plane-wave AVO inversion results.

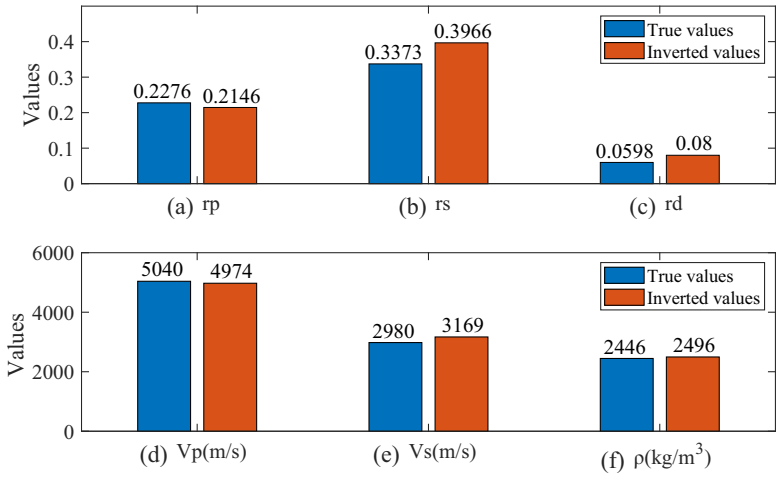

Figure 14. The spherical-wave AVO inversion results with noise (signal-to-noise ratio is 4).

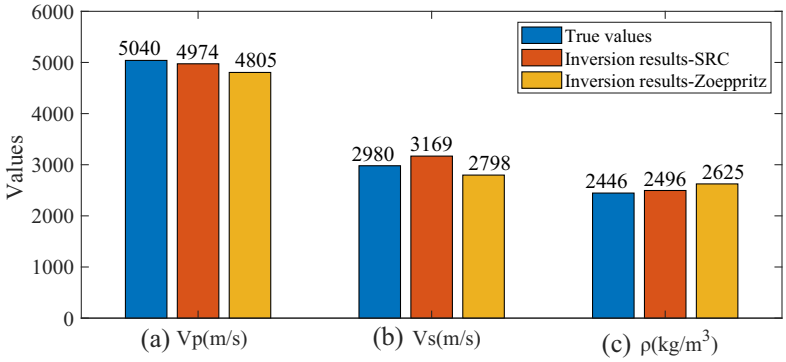

Figure 15. The comparison between the spherical-wave AVO inversion results and the plane-wave AVO inversion results based on Zoeppritz equation with noise.

6 FIELD DATA EXAMPLES

In the current research, the single plane interface between two half-spaces is usually designed, but the spherical-wave AVO inversion method for multilayer elastic media has not been developed. In order to promote the practical application of spherical-wave AVO inversion, our method can be developed to estimate elastic parameters in multilayer elastic media. The convolutional model (Robinson 1985) is utilized at each frequency component. The objective function can be obtained and expressed as

$$F = \left\| \sum_{\omega=\mathrm{LF}}^{\mathrm{HF}} W(\omega) * R_{\mathrm{pp}}^{\mathrm{sph}}(\omega) - d_{\mathrm{obs}} \right\|_2^2 = \mathrm{G}(\mathbf{m}), \tag{15}$$

where the asterisk denotes convolution and d_{obs} is the seismic trace near the borehole.

Fig. 16 displays the spherical-wave AVO inversion results and filtered well logs at the well location. The well logs are from an exploration area of eastern China. The red curve and black curve represent the filtered well logs and spherical-wave AVO inversion results, respectively. It can be seen from Fig. 16 that the spherical-wave AVO inversion results at the known well location are in good agreement with the filtered well logs, which verifies the feasibility and practicability of our method.

It must be admitted that there is a long way to go for spherical wave AVO inversion in realistic seismic exploration. Anelastic situations and curved interfaces make the band-limited spherical wave AVO inversion much more complicated. In addition, the band-limited wavelet is extracted based on the assumption of plane wave fronts rather than spherical wave fronts in current AVO technology.

7 CONCLUSION

In the isotropic elastic media, we derive a novel three-parameter spherical-wave reflection coefficient that can improve the stability of spherical-wave AVO inversion by reducing the number of inverted elastic parameters. With the increase of frequency and propagating distance, the differences between the PRC and the SRC become more and more small. In addition, we derive the SRC within the Fresnel zone that has large errors at the near-critical incidence angles, but elsewhere it is accurate.

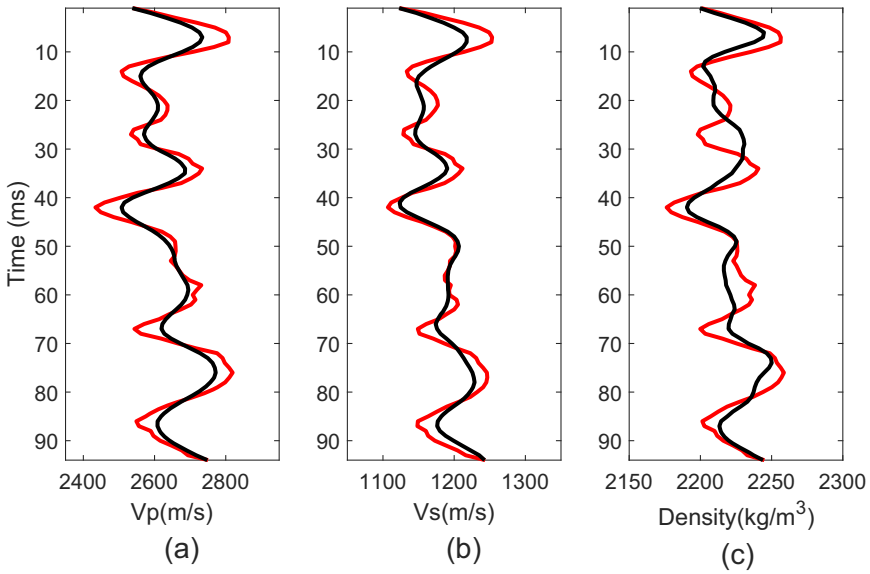

Figure 16. Spherical-wave AVO inversion results (black curves) and filtered well logs (red curves) at the known well location. (a) *P*-wave velocity, (b) *S*-wave velocity and (c) density.

The band-limited wavelet can be decomposed into the monochromatic spherical harmonic waves with different frequencies in the seismic frequency band. There is a one-to-one mapping between the SRC and its frequency component. The SRC can be regarded as the filter or weighting factor of the spherical waves. Elastic wave FD modelling demonstrates the accuracy and credibility of the spherical reflection waveform obtained by the inverse Fourier transform to the calculations for all frequency points.

We also propose the frequency-dependent spherical-wave AVO nonlinear inversion method that can make full use of the frequency components within the bandwidth of seismic data. We demonstrate the feasibility and robustness of our method by application on synthetic seismogram with white Gaussian noise. Furthermore, our method is applied to the estimation of elastic parameters of multilayer elastic media, and good inversion results are obtained through field data examples, which promotes the practical application of spherical-wave AVO inversion. Future work will include the spherical-wave AVO analysis and inversion for anelastic and anisotropy media.

ACKNOWLEDGEMENTS

We would like to acknowledge all the reviewers and editors and the sponsorship of National Science and Technology Major Project (2017ZX05009–001).

REFERENCES

Aki, K.T. & Richards, P.G., 2002. *Quantitative Seismology: Theory and Methods,* Vol. 1, University Science Books.

Alhussain, M., Gurevich, B. & Urosevic, M., 2008. Experimental verification of spherical-wave effect on the AVO response and implications for three-term inversion, *Geophysics,* **73,** C7–C12.

Ayzenberg, M., Tsvankin, I., Aizenberg, A. & Ursin, B., 2009. Effective reflection coefficients for curved interfaces in transversely isotropic media, *Geophysics,* **74,** WB33–WB53.

Berenger, J.P., 1994. A perfectly matched layer for the absorption of electromagnetic waves, *J. Comput. Phys.,* **114,** 185–200.

Bortfeld, R., 1961. Approximations to the reflection and transmission coefficients of plane longitudinal and transverse waves, *Geophys. Prospect.,* **9,** 485–502.

Brekhovskikh, L.M., 1980. *Waves in Layered Media,* Academic Press.

Buland, A. & Omre, H., 2003. Bayesian linearized AVO inversion, *Geophysics,* **68,** 185–198

Castagna, J.P. & Swan, H.W., 1997. Principles of AVO crossplotting, *Leading Edge,* **16,** 337–344.

Červený, V., 1959. On the reflection of spherical waves at a plane interface with refractive index near to one. I, *Stud. Geophys. Geod.,* **3,** 116–134.

Červený, V. & Hron, F., 1961. Reflection coefficients for spherical waves, *Stud. Geophys. Geod.,* **5,** 122–132.

Cheng, G., Yin, X. & Zong, Z., 2017. Nonlinear amplitude-variation-with-offset inversion for Lamé parameters using a direct inversion method, *Interpretation,* **5,** SL57–SL67.

Cheng, G., Yin, X. & Zong, Z., 2018. Third-order AVO inversion for lamé parameter based on inverse operator estimation algorithm, *J. Pet. Sci. Eng.,* **164,** 117–126.

Cheng, G., Yin, X. & Zong, Z., 2019. Nonlinear elastic impedance inversion in the complex frequency domain based on an exact reflection coefficient, *J. Pet. Sci. Eng.,* **178,** 97–105.

Favretto-Cristini, N., Cristini, P. & deBazelaire, E., 2007. Influence of the interface Fresnel zone on the reflected *P*-wave amplitude modelling, *Geophys. J. Int.,* **171,** 841–846.

Goertz, A., Milligan, P., Karrenbach, M. & Paulsson, B., 2005. Optimized 3D VSP survey geometry based on Fresnel zone estimates, *SEG Tech. Prog. Expanded Abstracts,* 2641–2644.

Goodway, B., Chen, T. & Downton, J., 1997. Improved AVO fluid detection and lithology discrimination using Lamé petrophysical parameters; "$\lambda\rho$", "$\mu\rho$", & "λ/μ fluid stack", from P and S inversions, *SEG Tech. Prog. Expanded Abstracts,* 183–186.

Haase, A.B., 2004. Spherical wave AVO modeling of converted waves in isotropic media, *SEG Tech. Prog. Expanded Abstracts,* 263–266.

Haase, A.B. & Ursenbach, C.P., 2006. Spherical-wave AVO modeling in elastic and anelastic media. *CREWES Res. Rep.,* **18,** 1–18.

Haase, A.B. & Ursenbach, C.P., 2007. Spherical-wave computational AVO modelling in elastic and anelastic isotropic two-layer media, in *69th Annual Conference and Exhibition, EAGE, Extended Abstracts,* doi:10.3997/2214-4609.201401971.

Krail, P. M. & Brysk, H., 1983. Reflection of spherical seismic waves in elastic layered media, *Geophysics,* **48,** 655–664.

Kroode, F.T., Bergler, S., Corsten, C, Maag, J.W., Strijbos, F. & Tijhof, H., 2013. Broadband seismic data—the importance of low frequencies, *Geophysics,* **78,** WA3–14.

Kumar, M., Barak, M.S. & Kumari, M., 2019. Reflection and refraction of plane waves at the boundary of an elastic solid and double-porosity dual-permeability materials, *Pet. Sci.,* **16**(2), 72–91.

Li, J.N., Wang, S.X., Tao, Y.H., Dong, C.H. & Tang, G.Y., 2017a. A novel expression of the spherical-wave reflection coefficient at a plane interface, *Geophys. J. Int.,* **211,** 700–717.

Li, J.N., Wang, S.X., Wang, J.B., Dong, C.H. & Yuan, S.Y., 2017b. Frequency dependent spherical-wave reflection characteristics in acoustic media, *Pure appl. Geophys.,* **174,** 1759–1778.

Li, L., Zhang, J.J., Pan, X.P. & Zhang, G.Z., 2020. Azimuthal elastic impedance-based Fourier coefficient variation with angle inversion for fracture weakness, *Pet. Sci.,* **17**(1), 86–104.

Ostrander, W.J., 1984. Plane-wave reflection coefficients for gas sands at nonnormal angles of incidence, *Geophysics,* **49,** 1637–1648.

Robinson, E.A., 1985. Seismic time-invariant convolutional model, *Geophysics,* **50**(12), 2742–2751.

Russell, B.H., Gray, D. & Hampson, D.P., 2011. Linearized AVO and poroelasticity, *Geophysics* **76,** C19–C29.

Rutherford, S.R. & Williams, R.H., 1989. Amplitude-versus-offset variations in gas sands, *Geophysics,* **54,** 680–688.

Růžek, B., Kolář, P. & Kvasnička, M., 2009. Robust solver of a system of nonlinear equations, *Technical Computing Prague,* **90,** 1–19.

Shampine, L.F., 2008. Vectorized adaptive quadrature in Matlab, *J. Comput. Appl. Math,* **211,** 131–140‖

Sheriff, R.E., 1980. Nomogram for Fresnel-zone calculation, *Geophysics,* **45,** 968–972.

Skopintseva, L., Ayzenberg, M., Landrø, M., Nefedkina, T. V. & Aizenberg, A.M, 2011. Long-offset AVO inversion of PP reflections from plane interface using effective reflection coefficients, *Geophysics,* **76**(6), C65–C79.

Smith, G.C. & Gidlow, P.M., 1987. Weighted stacking for rock property estimation and detection of gas, *Geophys. Prospect.,* **35,** 993–1014.

Sommerfeld, A., 1909. Über die Ausbreitung der Wellen in der drahtlosen Telegraphie, *Ann. Phys., Lpz.,* **333,** 665–736.

Spetzler, J. & Snieder, R., 2004. The Fresnel volume and transmitted waves, *Geophysics,* **69,** 653–663.

Stovas, A. & Ursin, B., 2003. Reflection and transmission responses of layered transversely isotropic viscoelastic media, *Geophys. Prospect.,* **51,** 447–477.

Ursenbach, C.P., Haase, A.B. & Downton, J. E., 2007. Efficient spherical-wave AVO modeling, *Leading Edge,* **26,** 1584–1589.

Ursin, B., Favretto-Cristini, N. & Cristini, P., 2014. Fresnel volume and interface Fresnel zone for reflected and transmitted waves from a curved interface in anisotropic media. *Geophysics,* **79**(5), C123–C134.

Wang, Y., 1999. Approximations to the Zoeppritz equations and their use in AVO analysis, *Geophysics,* **64,** 1920–1927.

Weyl, H., 1919. Ausbreitung elektromagnetischer Wellen ueber einem ebenen Leiter, *Ann. Phys. Lpz.,* **365,** 481–500.

Yilmaz, Ö., 2001. *Seismic Data Analysis: Processing, Inversion, and Interpretation Of Seismic Data,* Vol. 2, Society of Exploration Geophysicists.

Yin, X.Y. & Zhang, S.X, 2014. Bayesian inversion for effective pore-fluid bulk modulus based on fluid-matrix decoupled amplitude variation with offset approximation, *Geophysics,* **79,** R221–R232.

Yin, X.Y., Cheng, G.S. & Zong, Z.Y., 2018. Non-linear AVO inversion based on a novel exact PP reflection coefficient, *J. Appl. Geophys.,* **159,** 408–417.

Zhu, X.F. & McMechan, G.A., 2012. Elastic inversion of near and post-critical reflections using phase variation with angle, *Geophysics,* **77,** R149–R159.

Zoeppritz, K., 1919. On the reflection and penetration of seismic waves through unstable layers, *Göttinger Nachr.,* **1,** 66–84.

Zong, Z.Y., Yin, X.Y. & Wu, G.C., 2015. Complex seismic amplitude inversion for P-wave and S-wave quality factors, *Geophys. J. Int.,* **202,** 564–577.

Zong, Z.Y., Yin, X.Y., Zhu, M., Du, J.Y., Chen, W.T. & Zhang, W.W., 2017. Broadband seismic amplitude variation with offset inversion, *Geophysics,* **82,** M43–M53.

Zong, Z.Y., Wang, Y.R., Li, K. & Yin, X.Y., 2018. Broadband seismic inversion for low-frequency component of the model parameter, *IEEE Trans. Geosci. Remote Sens.,* **99,** 1–8.